mater.scichina.com link.springer.com

Sci China Mater 2025, 68(1): 189–198
https://doi.org/10.1007/s40843-024-3190-7

Boosting hydrogen evolution via work-function-accelerated electronic reconfiguration of Mo-based heterojunction

Xiang Chen[1], Shuai Feng[1], Song Xie[1], Yaping Miao[3], Biao Gao[4], Xuming Zhang[4], Li Huang[5], Yun Li[5], Paul K. Chu[2] and Xiang Peng[1*]

ABSTRACT Molybdenum-based catalysts have demonstrated significant potential in the electrocatalytic hydrogen evolution reaction (HER). However, the limited exposure of active sites and strong hydrogen adsorption result in suboptimal performance. Herein, a Mo_2N–$MoSe_2$ heterojunction is prepared on carbon cloth (MNS/CC) to enhance the HER. The strong electronic interaction between Mo_2N and $MoSe_2$, combined with the lower work function of Mo_2N, creates an intrinsic electric field at the heterojunction interface, which markedly improves charge transfer efficiency. Additionally, the optimized electronic structure of Mo sites further enhances charge transfer and intrinsically catalytic activity in HER. As a result, MNS/CC requires overpotentials of mere 65 and 210 mV to achieve current densities of 20 mA cm^{-2} and 1 A cm^{-2}, respectively, with a Tafel slope of only 96 mV dec^{-1}. Moreover, MNS/CC maintains stable operation at 1 A cm^{-2} for 240 h without significant degradation. The results offer insights into the design of non-precious metal-based electrocatalysts for industrial hydrogen production.

Keywords: water splitting, hydrogen evolution reaction, molybdenum-based catalyst, heterojunction, electronic interaction

INTRODUCTION

The increasing urgency to address depleting energy resources and mitigate global climate change caused by fossil fuels has spurred the development of clean hydrogen energy. The electrocatalytic hydrogen evolution reaction (HER) offers a sustainable and promising approach to hydrogen production [1,2]. However, the commercialization of HER has been constrained by the intrinsic scarcity and high expense of precious metal catalysts, including Pt and Pd [3,4]. In this respect, progress has been made in the exploration of non-noble transition metal compounds as efficient HER catalysts, including oxides [5–7], nitrates [8,9], chalcogenides [4,10–12], and carbides [13–15]. Among these, molybdenum diselenide ($MoSe_2$), a prominent transition metal chalcogenide, has drawn substantial interest due to its tunable active sites and outstanding stability [16,17]. However, the catalytic efficiency of $MoSe_2$ in HER is compromised by excessively strong hydrogen adsorption, limited exposure to active sites, and its semiconducting characteristics [18]. To overcome these limitations, heterointerface engineering has emerged as a promising strategy by activating inert surface atoms and improving the intrinsic electrocatalytic activity [19,20].

For instance, Patel *et al.* [21] have developed $MoSe_2$@WSe_2 by liquid exfoliation and electrophoretic deposition. This strategy increases the exposure of catalytic active sites at the nanocrystal edges, while the electronic interactions at the $MoSe_2$ and WSe_2 heterointerface significantly enhance the electrocatalytic activity for HER. As a result, the system achieves a current density of 10 mA cm^{-2} with an overpotential of 158 mV. Zong *et al.* [22] have employed titanium nitride (Ti_2NT_x) MXene as a two-dimensional substrate to synthesize nickel-doped $MoSe_2$ and Ti_2NT_x MXene nanocomposites (Ni–$MoSe_2$/Ti_2NT_x). This approach not only increases the exposure of active sites by preventing $MoSe_2$ agglomeration but also optimizes the electronic structure at the $MoSe_2$ and Ti_2NT_x interface, thereby enhancing electrocatalytic activity. In an alkaline medium, the Ni–$MoSe_2$/Ti_2NT_x catalyst achieves a current density of 10 mA cm^{-2} with an overpotential of 92 mV. Despite the crucial role of nitride- and selenide-based heterojunctions in modulating the electronic structure of active Mo sites to optimize Mo–H bonding during the HER, there remain challenges pertaining to the design of controllable synthesis strategies, especially *in-situ* synthesis of Mo-based nitride and selenide heterojunctions. Furthermore, the electronic interaction and electrocatalytic capability of these *in-situ* generated heterojunctions are not yet well understood.

Herein, a Mo_2N–$MoSe_2$ heterojunction was fabricated on carbon cloth (MNS/CC) via a chemical vapor deposition (CVD) technique. The heterojunction was formed by selenizing Mo_2N, which was derived from the ammonia nitridation of a MoO_3 precursor (Scheme 1). Experimental and theoretical approaches were employed to investigate the electronic interactions between

[1] Hubei Key Laboratory of Plasma Chemistry and Advanced Materials, Engineering Research Center of Phosphorus Resources Development and Utilization of Ministry of Education, School of Materials Science and Engineering, Wuhan Institute of Technology, Wuhan 430205, China
[2] Department of Physics, Department of Materials Science and Engineering, and Department of Biomedical Engineering, City University of Hong Kong, Hong Kong 999077, China
[3] School of Textile Science and Engineering, Xi'an Polytechnic University, Xi'an 710048, China
[4] The State Key Laboratory of Refractories and Metallurgy, Institute of Advanced Materials and Nanotechnology, Wuhan University of Science and Technology, Wuhan 430081, China
[5] Guizhou Wujiang Hydropower Development Co., Ltd., Guiyang 550002, China
* Corresponding author (email: xpeng@wit.edu.cn)

Mo_2N and $MoSe_2$ at the heterogeneous interface. The lower work function of Mo_2N, in conjunction with $MoSe_2$, establishes a built-in electric field that facilitates the efficient and spontaneous electron transfer from Mo_2N to $MoSe_2$. The optimized electronic structure of Mo sites improves charge transfer and intrinsic HER activity as well. As a result, MNS/CC has outstanding electrocatalytic properties, including overpotentials as low as 65 and 210 mV at current densities of 20 mA cm^{-2} and 1 A cm^{-2}, respectively. The low Tafel slope of 96 mV dec^{-1} indicates fast catalytic kinetics.

EXPERIMENTAL SECTION

Materials preparation

0.75 g of ammonium molybdate ($(NH_4)_2MoO_4$) was dissolved in deionized water (DW) (10 mL), which was then heated up to 70°C in a water bath and 40 mL of concentrated nitric acid (HNO_3) was poured in when the temperature was constant. The pretreated CC (2.5 × 2.5 cm^2) was supported in the solution for 0.5 h. Subsequent rinsing of the CC in a slow-flowing DW to remove surface impurities yielded the MoO_3/CC precursor. The MoO_3/CC precursor was subjected to annealing at 700°C in an ammonia atmosphere for 2 h, resulting in the formation of Mo_2N/CC (designated as MN/CC).

The prepared MN/CC was positioned downstream in the tube furnace, while 1.00 g of Se powder was placed upstream. The upstream section was then heated to 450°C in an N_2/H_2 atmosphere (containing 8% H_2). The resulting samples obtained at 400 and 600°C were Mo_2N–$MoSe_2$/CC (designated as MNS/CC) and $MoSe_2$/CC (designated as MS/CC), respectively.

Materials characterization

X-ray diffraction (XRD, LabX XRD-6100, Shimadzu) was used for phase composition determination. The surface morphology was characterized, and the elemental composition was quantified using a field emission scanning electron microscope (FE-SEM, Gemini 300), a transmission electron microscope (TEM, JEOL JEM-F200), and energy-dispersive X-ray spectroscopy (EDS). High-resolution TEM (HR-TEM) was employed to identify the crystal structure and lattice spacing. X-ray photoelectron spectroscopy (XPS, Thermo Scientific ESCALAB 250Xi) with monochromatic Al Kα radiation was employed to analyze the chemical states of the sample surface. The specific surface area of the samples was calculated from the N_2 adsorption-desorption isotherms through the Branauer-Emmett-Teller (BET) equation using a micromeritics TriStar II Plus analyzer. The Mo mass loading of the electrodes was determined by an inductively coupled plasma spectrometer (ICP, Thermo Scientific iCAP PRO).

Electrochemical measurement

Electrochemical measurements were performed using a three-electrode configuration on a CHI 760E electrochemical workstation (Shanghai CH Instrument, China). A saturated calomel electrode (SCE) served as the reference electrode, while a graphite rod was used as the counter electrode. The working electrode was a CC modified with the electrocatalyst. All potentials were calibrated with respect to the reversible hydrogen electrode (RHE) using the Nernst equation: $E_{RHE} = E_{SCE} + 0.242 + 0.059 \times$ pH. The electrolyte employed was 0.5 M H_2SO_4, with the pH measured as 0.56 using a pH meter (FE28, Mettler Toledo). Linear sweep voltammetry (LSV) was conducted at a scanning rate of 5 mV s^{-1} with *iR*-compensation. The Tafel slope was calculated according to the formula $\eta = a + b\log|j|$, where η represents the overpotential, a is constant, b is the Tafel slope, and j is the current density. The electrochemical impedance spectroscopy (EIS) was performed at an initial potential of −0.48 V vs. SCE, spanning a frequency range from 100 kHz to 0.1 Hz with a 5 mV amplitude. The electrochemically active surface area (ECSA) was evaluated using cyclic voltammetry (CV) within a potential range of −0.15 to −0.05 V vs. SCE, with scan rates varying from 10 to 70 mV s^{-1}. The stability of the catalyst was evaluated using chronoamperometry (CP), with the actual H_2 production quantified using the drainage method.

Density functional theory calculations

Density Functional Theory (DFT) calculations, based on first principles, were performed using the Generalized Gradient Approximation (GGA) and the Perdew-Burke-Ernzerhof (PBE) exchange-correlation functional, with a cutoff energy of 290 eV. The structures were optimized until the atomic forces were below 0.03 eV $Å^{-1}$, which was sufficient to avoid interactions between adjacent structures. The total energy convergence criterion was set to 1.0 × 10^{-5} eV per atom. The surface and adsorbate layers were allowed to relax, while the bottom atoms were held fixed to eliminate internal stresses within the system.

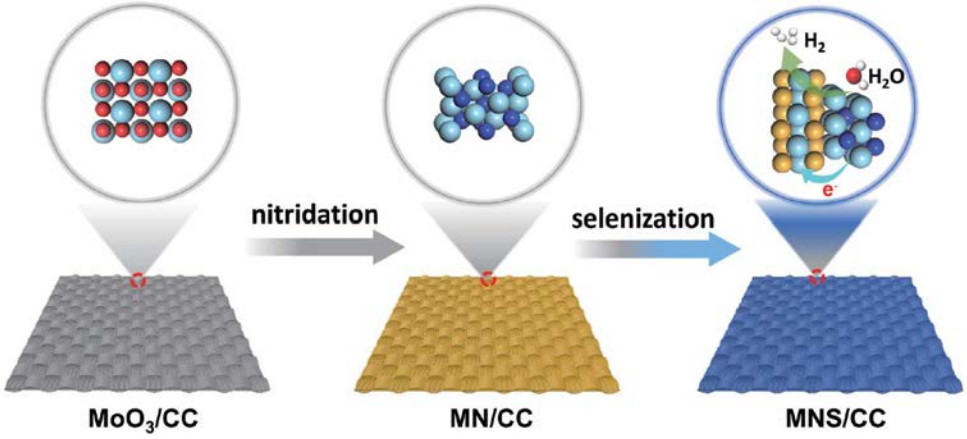

Scheme 1 Construction of Mo_2N–$MoSe_2$ heterojunction on CC for boosting hydrogen evolution.

A 3 × 2 × 1 *k*-point grid and a cutoff energy of 300 eV were employed for all calculations. A 15 Å vacuum layer was added to prevent interactions along the *z*-direction.

The hydrogen adsorption capability of the catalysts was evaluated using the hydrogen adsorption free energy (ΔG_{H^*}) proposed by Nørskov *et al.* [23], a crucial parameter for HER activity. The structures with H groups adsorbed on $Mo_2N(111)$, $MoSe_2(002)$, and $Mo_2N(111)$–$MoSe_2(002)$ were constructed and optimized. The adsorption-free energy was computed using the following method:

$$\Delta E_{H^*} = E_{(slab\ +\ H^*)} - E_{(slab)} - E_{H}, \quad (1)$$

$$\Delta G_{H^*} = \Delta E_{H} + \Delta E_{ZPE} - T\Delta S, \quad (2)$$

where $E_{(slab\ +\ H^*)}$ denotes the total energy of hydrogen adsorbed on the catalyst surface, ΔE_{H^*} represents the adsorption energy of hydrogen, and E_H and $E_{(slab)}$ correspond to the energies of the isolated hydrogen atom and the clean catalyst, respectively. ΔG_{H^*} denotes the hydrogen adsorption free energy, ΔE_{ZPE} represents the zero-point energy, ΔS signifies the entropy change, and T denotes the temperature, where $\Delta E_{ZPE} - T\Delta S$ being 0.24 eV [24,25].

RESULTS AND DISCUSSION

Morphology and structure

Fig. 1a illustrates the synthesis of the MNS/CC electrocatalyst. The MoO_3 nanowire arrays are grown on CC by a wet chemistry method and subsequent ammonia annealing converts MoO_3 into Mo_2N, with NH_3 being the nitrogen source. A programmed heating protocol was then employed to introduce Se into Mo_2N to produce mixed phases of Mo_2N and $MoSe_2$. The gradual transition from Mo_2N to $MoSe_2$ creates a heterointerface composed of Mo_2N and $MoSe_2$, which likely modulates the electronic structure and enhances the electrocatalytic activity.

The FE-SEM images in Fig. 1b, c reveal nanowire arrays surrounding the carbon fiber scaffold of MoO_3/CC. After the annealing in NH_3 at 700°C, the nanowire array is preserved, as shown in Fig. S1. Subsequent introduction of Se powder by thermal treatments at 400 and 600°C maintains the nanowire array morphology with negligible deviation from the initial structure, as demonstrated in Fig. 1d, e and Fig. S2.

The phase composition and crystal structure were analyzed

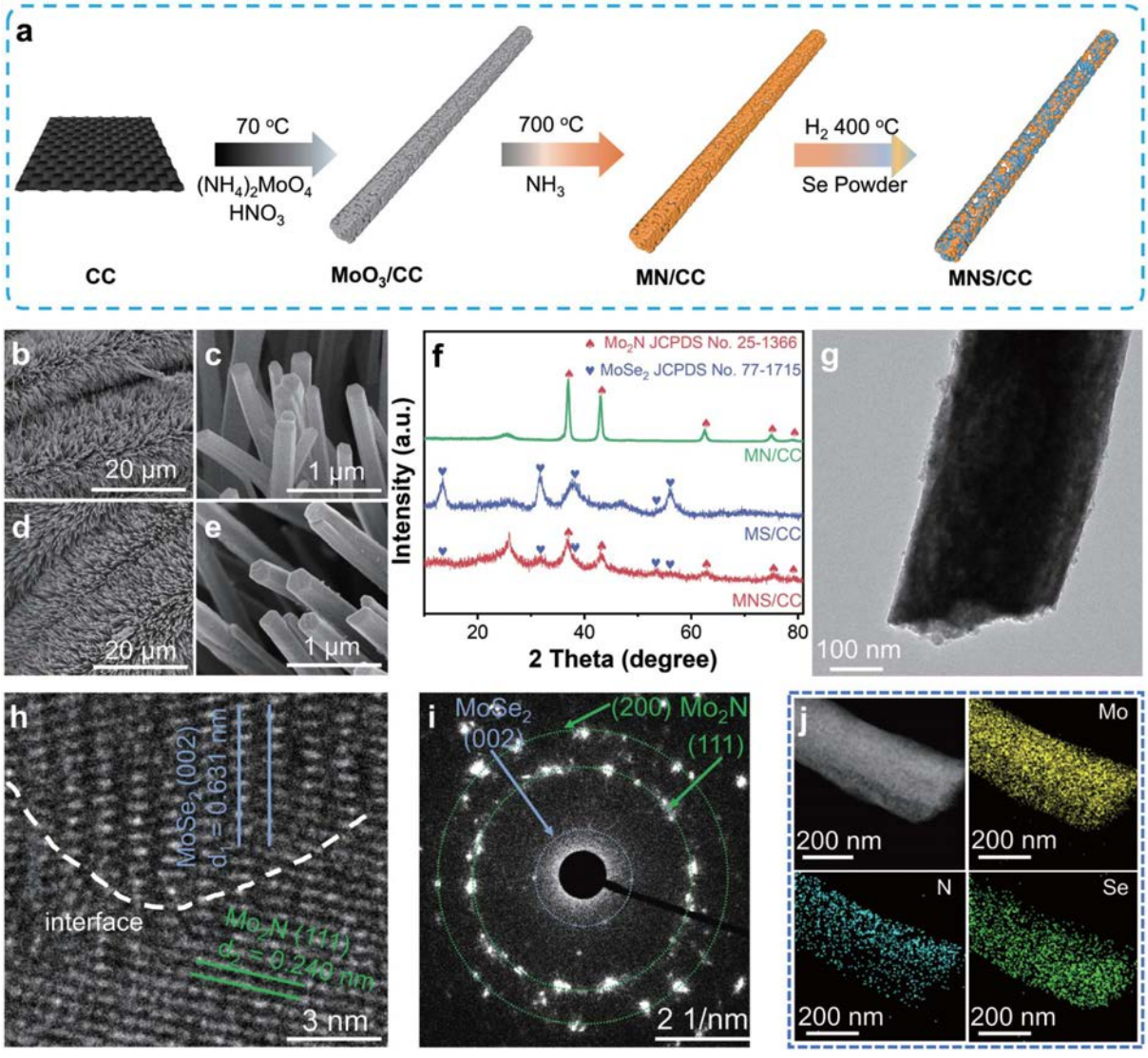

Figure 1 (a) Schematic of MNS/CC electrocatalyst preparation; FE-SEM images of (b, c) MoO_3/CC and (d, e) MNS/CC; (f) XRD patterns of MN/CC, MS/CC, and MNS/CC; (g) TEM image, (h) HR-TEM image, (i) SAED pattern, and (j) Element maps of Mo, N, and Se of MNS/CC.

using XRD. The diffraction peaks of the product obtained by the solution method (Fig. S3) match the (210), (300), (310), (410), (500), and (218) planes of hexagonal MoO_3 (JCPDS card No. 21-0569), confirming the synthesis of pure phase MoO_3. The XRD pattern after ammonia annealing at 700°C shows peaks at 37.4°, 43.5°, 63.1°, 75.7°, and 79.7°, corresponding to the (111), (200), (220), (311), and (222) planes of cubic Mo_2N (JCPDS card No. 25-1366), respectively, as shown in Fig. 1f (green line). After introducing Se into Mo_2N via heating at 400°C, additional peaks at 13.7°, 31.4°, 37.8°, 53.3° and 55.9° corresponding to the (002), (100), (103), (106), and (110) planes of hexagonal $MoSe_2$ (JCPDS card No. 77-1715), respectively, are shown in Fig. 1f (red line). This confirms the successful synthesis of a mixed-phase composite comprising Mo_2N and $MoSe_2$. However, at an annealing temperature of 600°C with Se powder, the Mo_2N diffraction peaks disappear, leaving only the peaks of $MoSe_2$, as shown in Fig. 1f (blue line). This demonstrates that the formation of $MoSe_2$ involves the *in-situ* phase transition from Mo_2N to $MoSe_2$, resulting in the presence of both phases.

The TEM image discloses the nanowire morphology of MNS, as shown in Fig. 1g, which facilitates charge transfer and exposes a larger surface area for electrocatalytic reactions. As shown in Fig. 1h, the lattice spacings, obtained from HR-TEM images, are 0.240 and 0.631 nm, corresponding to the (111) plane of Mo_2N and the (002) plane of $MoSe_2$, respectively. These Mo_2N(111) and $MoSe_2$(002) planes are misaligned, thus creating a distinct heterogeneous interface between them, as indicated by the dotted line and suggesting the formation of a Mo_2N–$MoSe_2$ heterointerface after the selenization of Mo_2N. The heterointerface induces electronic interactions between the phases, resulting in a built-in electric field that accelerates the kinetics of electrocatalytic reactions. Furthermore, it modifies the electronic structure of molybdenum atoms, thereby activating the intrinsic electrocatalytic capability. The selected-area electron diffraction (SAED) image in Fig. 1i provides evidence of the presence of Mo_2N and $MoSe_2$, consistent with HR-TEM and XRD. The elemental mappings of MNS, shown in Fig. 1j, reveal the uniform distribution of Mo, N, and Se within the nanowires. The BET surface area analysis in Fig. S4 indicates the similar specific surface area of the catalysts.

The chemical state of the heterointerface was determined using XPS. The surface survey spectra in Fig. 2a exhibit distinct peaks corresponding to Mo, N, and Se elements in MNS/CC. No nitrogen signal is detected from MS/CC after annealing at 600°C with a Se source, indicating the complete conversion of Mo_2N to $MoSe_2$. The Mo-3d spectra in Fig. 2b display peaks corresponding to Mo-$3d_{5/2}$ and Mo-$3d_{3/2}$ of the Mo–Se species at approximately 229.3 and 232.4 eV, respectively, while the peaks at 228.5 and 231.6 eV correspond to Mo-$3d_{5/2}$ and Mo-$3d_{3/2}$ of Mo–N species [26,27]. The peak at 230.6 eV corresponds to Se-3s [28]. The ratio of Mo–N/Mo–Se of MNS/CC is calculated to be 0.16. In MNS/CC, the binding energy of the Mo–Se bond decreases by 0.25 eV compared to pure-phase MS/CC, while the Mo–N bond's binding energy increases by 0.29 eV relative to

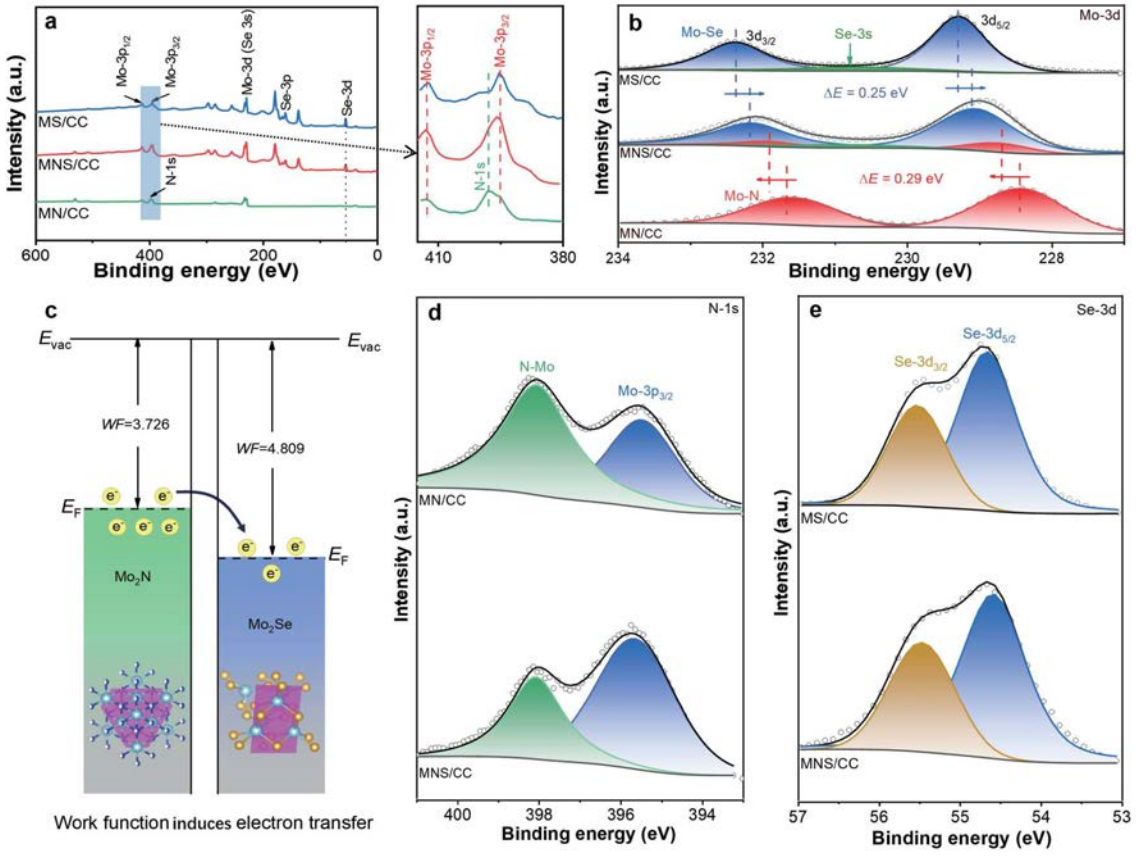

Figure 2 (a) XPS survey spectra and a magnified view within the 380–415 eV range. (b) High-resolution Mo-3d XPS spectra of MN/CC, MNS/CC, and MS/CC, respectively. (c) Schematic diagram of electron transfer at the interface with E_F and E_{vac} denoting the Fermi level and vacuum level, respectively. High-resolution XPS spectra of MN/CC, MNS/CC, and MS/CC: (d) N-1s and (e) Se-3d.

pure-phase MN/CC. These observations suggest electronic reconstruction at the Mo_2N–$MoSe_2$ heterointerface, where electrons are transferred from Mo_2N to $MoSe_2$.

To study electron transfer between Mo_2N and $MoSe_2$ at the Mo_2N–$MoSe_2$ heterointerface, the energy diagrams of Mo_2N, $MoSe_2$, and Mo_2N–$MoSe_2$ are calculated and presented in Fig. 2c and Fig. S5. The work function of Mo_2N–$MoSe_2$ is 4.102 eV, while Mo_2N and $MoSe_2$ are 3.726 and 4.809 eV, respectively, implying that electrons move spontaneously from Mo_2N to $MoSe_2$ at the heterointerface [29–31], with is consistent with XPS. Furthermore, the difference in work functions generates a built-in electric field, which facilitates charge transfer and accelerates the catalytic kinetics [32]. The N-1s spectra in Fig. 2d reveal that both MN/CC and MNS/CC exhibit a peak at 398.1 eV, indicating the presence of N–Mo bonds and confirming their association with Mo_2N [33]. In Fig. 2e, the Se-3d spectra of MNS/CC and MS/CC show binding energies of 55.6 and 54.7 eV, corresponding to the $3d_{5/2}$ and $3d_{3/2}$ states of $MoSe_2$, respectively [34].

Electrochemical evaluation

The HER properties are assessed in a 0.5 M H_2SO_4 using a three-electrode system. All potentials were *iR*-corrected unless otherwise specified to describe the intrinsically catalytic activity of the catalysts. Fig. 3a shows that the LSV curves demonstrate the exceptional performance of MNS/CC, including a current density of 20 mA cm^{-2} with a low overpotential of 65 mV, which surpasses MN/CC (192 mV), MS/CC (181 mV), and bare CC (517 mV), and approaches the overpotential of the commercial Pt/C catalyst (57 mV). MNS/CC exhibits a rapid increase in current density with applied potentials, achieving a current density of 1 A cm^{-2} with an overpotential of only 210 mV. This exceptional catalytic activity surpasses the performance of pure-phase MN/CC (703 mV) and MS/CC (912 mV), as shown in Fig. 3b. The LSV curves without *iR* compensation in Fig. S6 indicate the promising potential of the MNS/CC electrocatalyst for practical applications. The Tafel slope of MNS/CC is 96 mV dec^{-1}, which is lower than that of MN/CC (139 mV dec^{-1}), MS/CC (106 mV dec^{-1}), and bare CC (317 mV dec^{-1}), and is comparable to the commercial Pt/C catalyst (71 mV dec^{-1}), as shown in Fig. 3c. The small Tafel slope indicates that MNS/CC exhibits enhanced HER kinetics [35].

The ECSA is used to assess the intrinsic activity of electrocatalysts. ECSA is determined from the double-layer capacitance (C_{dl}) derived from CV curves in the non-Faradic region, as shown in Fig. S7. Among all the catalysts, MNS/CC exhibits the highest C_{dl} of 336 mF cm^{-2} (Fig. 3d), indicating a significantly larger ECSA for HER and a greater number of exposed active sites [36]. The ECSA-normalized LSV curves in Fig. 3e further illustrate the exceptional intrinsic electrocatalytic capability of MNS/CC compared to the pure phase MN/CC and MS/CC catalysts. The mass activity was calculated based on Mo mass

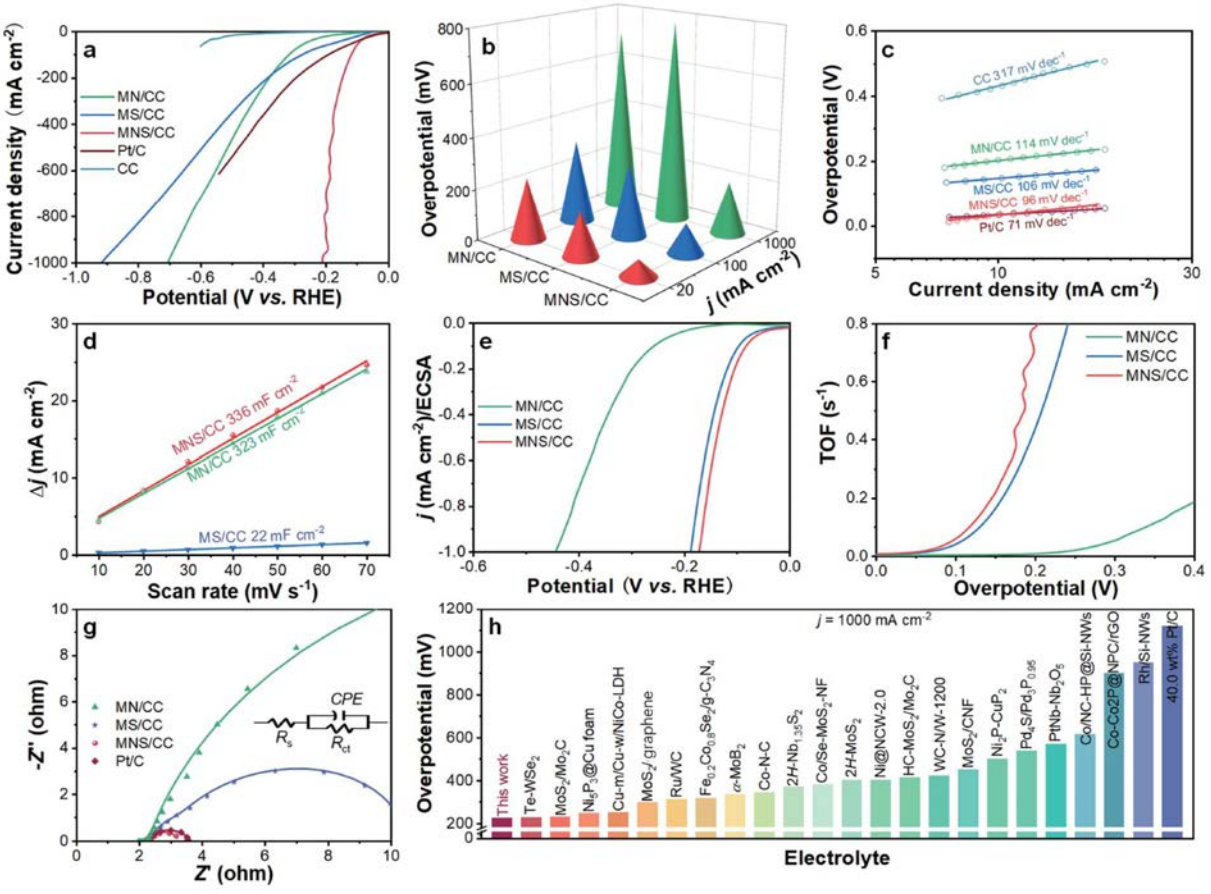

Figure 3 HER properties of the catalysts in 0.5 M H_2SO_4. (a) LSV curves with *iR* compensation. (b) Overpotentials for current densities of 20, 100, and 1 A cm^{-2}. (c) Tafel plot. (d) ECSA. (e) ECSA normalized LSV curves. (f) TOF. (g) EIS. (h) Comparison of the overpotential required for MNS/CC at a current density of 1 A cm^{-2} with those of other advanced electrocatalysts reported in the literature.

loading on the electrode, which was determined by ICP, as shown in Table S1. As shown in Fig. S8, Mo_2N/CC, MNS/CC, and $MoSe_2$/CC required overpotentials of 576, 198, and 702 mV, respectively, to achieve a current density of 100 mA mg_{Mo}^{-1}. These results indicate that MNS/CC exhibits superior HER catalytic performance. The intrinsic activity of the electrocatalysts for HER is also assessed using turnover frequency (TOF), defined as the turnover rate per active site for HER, which effectively normalizes the catalytic activity for different catalyst [36]. As shown in Fig. 3f, at an overpotential of 200 mV, the TOF value of MNS/CC (0.79 s^{-1}) exceeds that of pure MN/CC (0.01 s^{-1}) and MS/CC (0.43 s^{-1}) catalysts. The larger TOF is attributed to the Mo_2N–$MoSe_2$ heterointerface, which modifies the electronic structure and generates an internal electric field, facilitating rapid charge transfer and enhancing HER.

The Nyquist plots are derived to determine the charge transfer resistance (R_{ct}) during HER, with a smaller radius indicating lower R_{ct}. Fig. 3g and Fig. S9 reveal that MNS/CC has a notably lower R_{ct}, suggesting rapid charge transfer, which aligns with the observed smaller Tafel slope. The HER properties, particularly the overpotential required to achieve a current density of 1 A cm^{-2}, of MNS/CC are compared with other reported transition metal-based nitrides, selenides, phosphides, sulfides, etc., including Te-WSe_2 (225 mV) [37], MoS_2/Mo_2C (227 mV) [38], Ni_5P_4@Cu foam (~230 mV) [39], Cu-m/Cu-w/NiCo-LDH (246 mV) [40], 2*H*-$Nb_{1.35}S_2$ (370 mV) [41], Co/Se-MoS_2-NF (382 mV) [42], MoS_2/graphene (250 mV) [43], Ru/WC (310 mV) [44], $Fe_{0.2}Co_{0.8}Se_2$/g-C_3N_4 (317 mV) [45], α-MoB_2 (334 mV) [46], WC-N/W-1200 (420 mV) [47], Ni@NCW-2.0 (401 mV) [48], HC-MoS_2/Mo_2C (412 mV) [49], Co-N-C (343 mV) [50], MoS_2/CNF (450 mV) [51], Ni_2P-CuP_2 (~500 mV) [52], Pd_4S/$Pd_3P_{0.95}$ (538 mV) [53], Co/NC-HP@Si-NWs (615 mV) [54], Co-Co_2P@NPC/rGO (900 mV) [55], Rh/Si-NWs (950 mV) [56], and 40.0 wt% Pt/C (1120 mV) [38], as shown in Fig. 3h and Table S2. This comparison highlights the superior intrinsic HER activity of MNS/CC.

The stability is a crucial factor in practice, and MNS/CC is assessed at a constant current density of 1 A cm^{-2} (Fig. 4a). Even after 240 h of continuous operation, the potential remained stable with no noticeable change. In addition, the LSV curves before and after the stability test in Fig. 4b reveal consistent behavior, confirming the excellent HER stability of MNS/CC. Additionally, a comparative analysis of the LSV curves before and after multiple CV tests reveals a strong consistency, as illustrated in Fig. S10. The morphology, structure, and chemical state of MNS/CC after the stability test are investigated. The FE-SEM images indicate that the nanowire array remains intact without showing detachment (Fig. 4c and Fig. S11). The XRD pattern of MNS/CC in Fig. 4d reveals both Mo_2N and $MoSe_2$ phases similar to the pristine sample. The high-resolution XPS Mo-3d spectrum of MNS/CC after the stability test is comparable to that of the original sample, with Mo–N/Mo–Se ratios around 0.16, as shown in Fig. 4e. These results confirm the long-

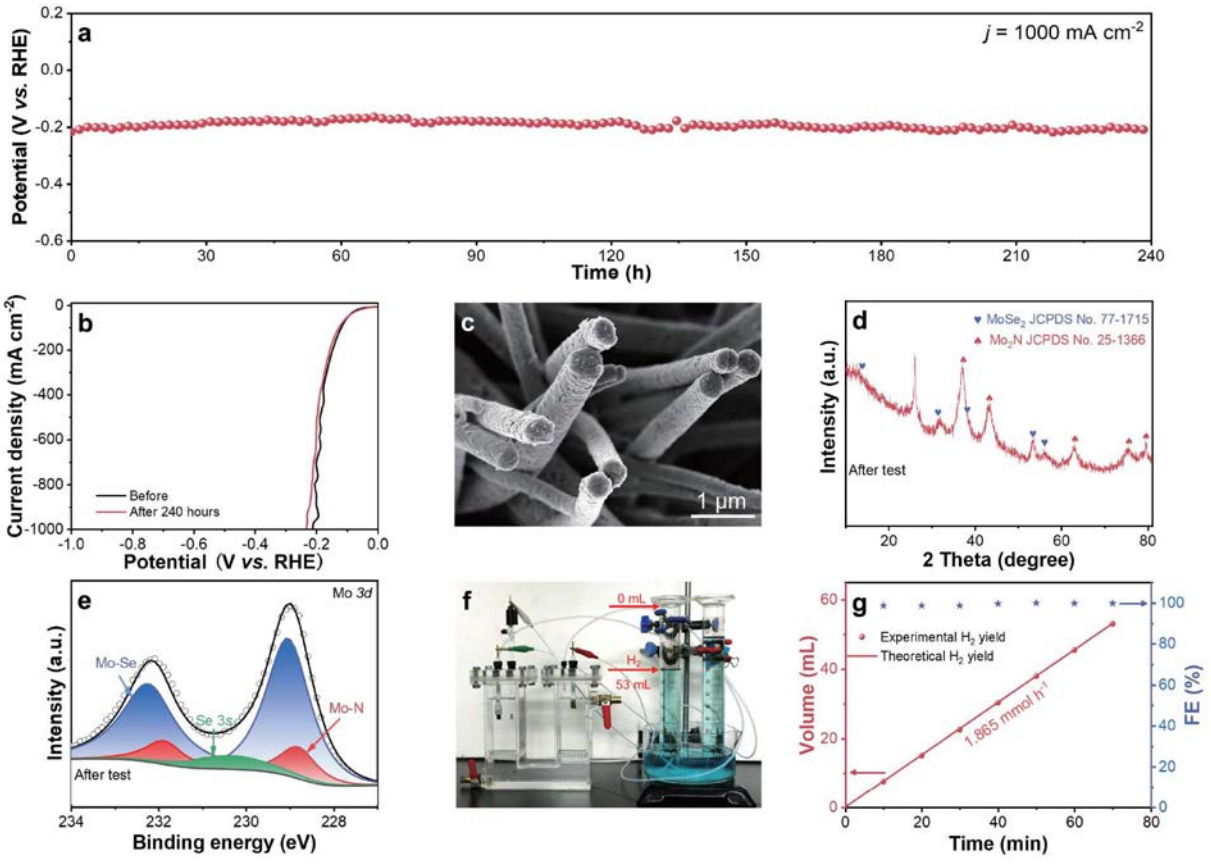

Figure 4 (a) Stability test of MNS/CC. (b) LSV curves before and after the stability test. (c) FE-SEM image, (d) XRD pattern, and (e) high-resolution Mo-3d XPS spectrum of MNS/CC after the long-term test. (f) Photograph of the H_2 production system using the water displacement method. (g) Experimental and theoretical volumes of H_2 produced and *FE* by MNS/CC at a current of 100 mA.

term durability of MNS/CC in acidic HER. The water displacement method, as illustrated in Fig. 4f, is used to determine the volume of hydrogen produced and the Faradic efficiency (*FE*) of MNS/CC during HER. A total of 53.0 mL of H_2 was produced within 70 min at a constant current of 100 mA, as shown in Fig. 4g. The hydrogen yield is calculated to be 1.865 mmol h^{-1}. *FE* represents the electron utilization efficiency of the catalyst and is a crucial indicator of commercial viability. The *FE* for hydrogen production is calculated to be 99.6% (Fig. 4g), indicative of an extremely high energy conversion efficiency.

DFT calculations

To elucidate the mechanism behind the catalytic activity enhancement of the Mo_2N–$MoSe_2$ heterointerface in HER, DFT calculations are performed. The models of Mo_2N(111), $MoSe_2$ (002), and the Mo_2N(111)–$MoSe_2$(002) heterointerface are constructed based on the HR-TEM and XRD results, as shown in Fig. S12. At the Mo_2N–$MoSe_2$ heterointerface, hydrogen adsorbs onto the Mo sites of both Mo_2N (H-MN@MNS) and $MoSe_2$ (H-MS@MNS), as shown in Fig. 5a, b. On the pure surfaces of Mo_2N and $MoSe_2$, hydrogen atoms adsorb onto the Mo sites labelled as H-MN and H-MS, respectively, as shown in Fig. 5c, d. The calculated band structures of Mo_2N, $MoSe_2$, and Mo_2N–$MoSe_2$ heterointerface in Fig. S13a–c reveal that the Mo_2N–$MoSe_2$ heterointerface has metallic properties, suggesting exceptional charge transfer efficiency in HER. The *d*-band centers of the models in Fig. 5e shows that the *d*-band centers of the Mo_2N–$MoSe_2$ heterointerface are located at −3.76 eV, which is significantly lower than those of pure Mo_2N (−3.51 eV) and $MoSe_2$ (−2.27 eV). This downshift of the *d*-band center at the Mo_2N–$MoSe_2$ heterointerface enhances the antibonding orbital, weakens H adsorption at the heterointerface, and expedites the release of hydrogen product [57,58]. As a result, the HER catalytic activity is enhanced.

The key parameter for predicting the HER activity of an electrocatalyst is the free energy of hydrogen adsorption (ΔG_{H^*}), with ΔG_{H^*} close to zero indicating a highly desirable electrocatalyst. Fig. 5f shows that both H-MN@MNS (−0.19 eV) and H-MS@MNS (−0.11 eV) have ΔG_{H^*} closer to zero than H-MN (−0.67 eV) and H-MS (−0.69 eV), suggesting that the Mo_2N–$MoSe_2$ heterointerface surface reduces Mo–H binding and thus accelerates hydrogen release. Furthermore, ΔG_{H^*} of H-MN@MNS (−0.19 eV) is sparser than zero than that of H-MS@MNS (−0.11 eV), indicating that the Mo sites in the $MoSe_2$ phase at the Mo_2N–$MoSe_2$ heterointerface are particularly effective in promoting HER by facilitating hydrogen release, thus serving as the active centers for HER.

Further insight into the catalytic mechanism of MNS/CC was gained by analyzing the projected density of states (PDOS) of

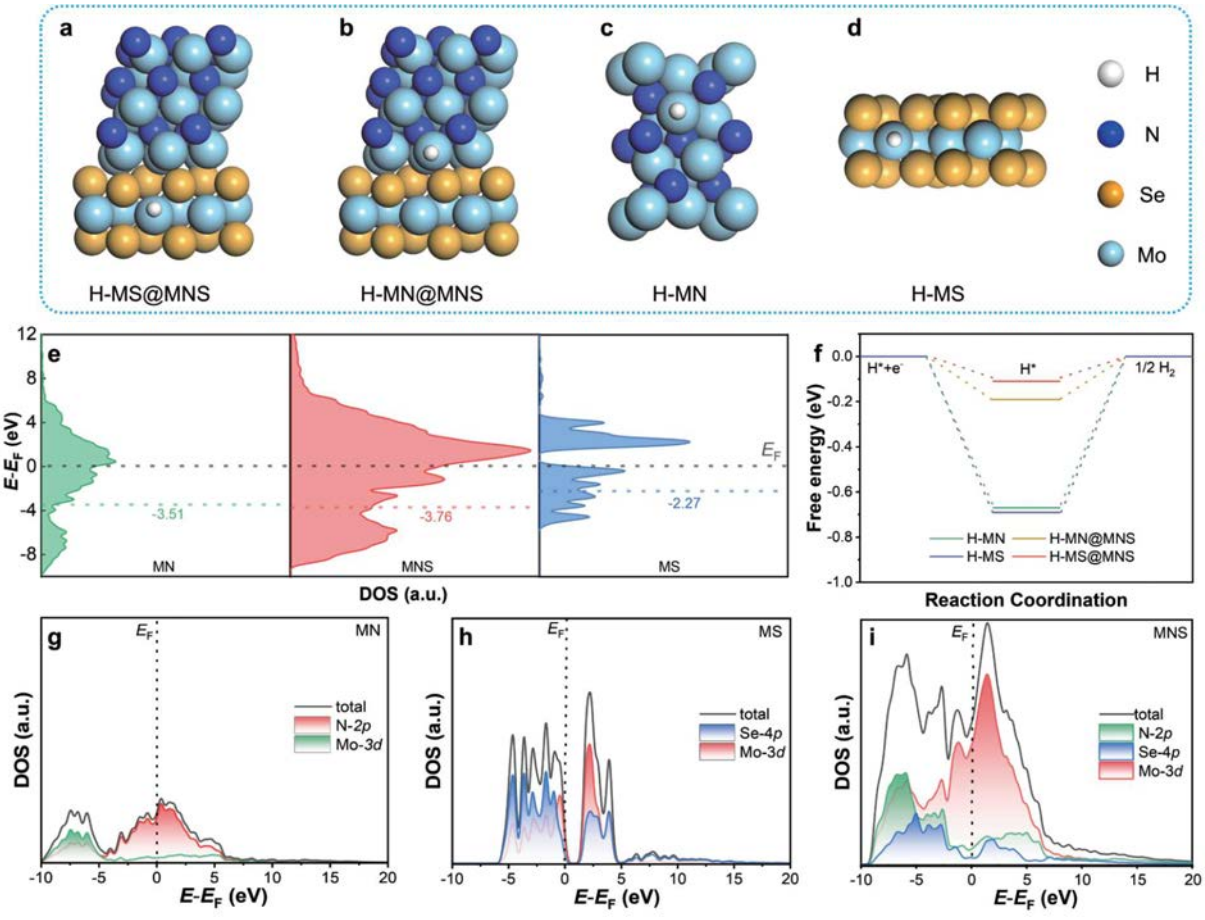

Figure 5 Optimized models for hydrogen adsorption on (a, b) Mo_2N–$MoSe_2$ heterointerface, (c) Mo_2N, and (d) $MoSe_2$. (e) *d*-band center of Mo_2N, $MoSe_2$–Mo_2N heterointerface, and $MoSe_2$. (f) Gibbs free energy diagram of Mo_2N, $MoSe_2$, and Mo_2N–$MoSe_2$ heterointerface. PDOS of (g) Mo_2N, (h) $MoSe_2$, and (i) Mo_2N–$MoSe_2$ heterointerface.

Mo_2N, $MoSe_2$ and Mo_2N–$MoSe_2$ heterogeneous surfaces. Fig. 5g–i reveals that the Mo_2N–$MoSe_2$ heterointerface exhibits enhanced hybridization between Mo-3d and N-2p orbitals at the Fermi level compared to the pure Mo_2N. Notably, the strengthened coupling between N-2p and Mo-3d at the Mo_2N–$MoSe_2$ heterointerface near the Fermi level produces strong electronic interactions to modulate the electronic configuration of the active sites. Additionally, the Mo-3d orbitals in the Mo_2N–$MoSe_2$ heterointerface shift towards the Fermi level, indicating efficient p-d electron transfer from the Se-4p orbitals to Mo-3d orbitals and strong electronic interactions between these two orbitals. The Mo_2N–$MoSe_2$ heterointerface exhibits more continuous and dense energy bands near the Fermi level than pure $MoSe_2$. These findings suggest improved intrinsic electrocatalytic capability and fast charge transfer at the Mo_2N–$MoSe_2$ heterointerface during HER.

CONCLUSIONS

A heterointerface comprised of Mo_2N and $MoSe_2$ is fabricated on carbon cloth by employing a two-step CVD technique, using MoO_3/CC as the precursor. Strong electronic interactions are observed between Mo_2N and $MoSe_2$ at the heterointerface. The lower work function of Mo_2N facilitates electron transfer from Mo_2N to $MoSe_2$, generating a built-in electric field that greatly enhances the charge transfer efficiency. Furthermore, the hybridization between N-2p/Se-4p and Mo-3d orbitals enhances charge transfer and the intrinsic electrocatalytic activity of MNS/CC in HER. As a result, MNS/CC demonstrates remarkable electrocatalytic performance, characterized by overpotentials of 65 mV at a current density of 20 mA cm^{-2} and 210 mV at 1 A cm^{-2}, respectively, a Tafel slope of 96 mV dec^{-1} indicative of efficient catalytic kinetics, and exceptional stability, as evidenced by continuous operation for 240 h at a current density of 1 A cm^{-2} with negligible degradation. The catalyst demonstrates a notable hydrogen production yield of 1.865 mmol h^{-1}, coupled with an exceptional Faraday efficiency of 99.6%. This study proposes an effective approach to designing Mo-based heterostructures for HER and sheds light on the advancement of non-precious metal electrocatalysts for industrial hydrogen production.

Received 23 September 2024; accepted 8 November 2024; published online 3 December 2024

1 Wang T, Tao L, Zhu X, *et al.* Combined anodic and cathodic hydrogen production from aldehyde oxidation and hydrogen evolution reaction. Nat Catal, 2022, 5: 66–73
2 Zhu J, Hu L, Zhao P, *et al.* Recent advances in electrocatalytic hydrogen evolution using nanoparticles. Chem Rev, 2020, 120: 851–918
3 Liu K, Yang H, Jiang Y, *et al.* Coherent hexagonal platinum skin on nickel nanocrystals for enhanced hydrogen evolution activity. Nat Commun, 2023, 14: 2424
4 Dai L, Fang C, Zhang X, *et al.* Multiscale confinement nitridation in molybdenum carbide for efficient hydrogen production. J Energy Chem, 2024, 94: 61–69
5 Zhai P, Zhang Y, Wu Y, *et al.* Engineering active sites on hierarchical transition bimetal oxides/sulfides heterostructure array enabling robust overall water splitting. Nat Commun, 2020, 11: 5462
6 Chen Z, Gong W, Wang J, *et al.* Metallic W/WO_2 solid-acid catalyst boosts hydrogen evolution reaction in alkaline electrolyte. Nat Commun, 2023, 14: 5363
7 Cui X, Sun Y, Xu X. Polyoxometalate derived p-n heterojunction for optimized reaction interface and improved HER. Chin Chem Lett, 2023, 34: 107348
8 Zhang Z, Fu Q, Xu K, *et al.* Intrinsically active surface in a Pt/γ–Mo_2N catalyst for the water-gas shift reaction: molybdenum nitride or molybdenum oxide? J Am Chem Soc, 2020, 142: 13362–13371
9 Li S, Wang S, He J, *et al.* Chromium-doped nickel oxide and nickel nitride mediate selective electrocatalytic oxidation of sterol intermediates coupled with H_2 evolution. Angew Chem Int Ed, 2023, 62: e202306553
10 Peng X, Xie S, Xiong S, *et al.* Ultralow-voltage hydrogen production and simultaneous Rhodamine B beneficiation in neutral wastewater. J Energy Chem, 2023, 81: 574–582
11 Chen X, Liu G, Zheng W, *et al.* Vertical 2D MoO_2/$MoSe_2$ core-shell nanosheet arrays as high-performance electrocatalysts for hydrogen evolution reaction. Adv Funct Mater, 2016, 26: 8537–8544
12 Li X, Zheng L, Liu S, *et al.* Heterostructures of NiFe LDH hierarchically assembled on MoS_2 nanosheets as high-efficiency electrocatalysts for overall water splitting. Chin Chem Lett, 2022, 33: 4761–4765
13 Huang C, Miao X, Pi C, *et al.* Mo_2C/VC heterojunction embedded in graphitic carbon network: an advanced electrocatalyst for hydrogen evolution. Nano Energy, 2019, 60: 520–526
14 Li Y, Dou Z, Pan Y, *et al.* Crystalline phase engineering to modulate the interfacial interaction of the ruthenium/molybdenum carbide for acidic hydrogen evolution. Nano Lett, 2024, 24: 5705–5713
15 Chen C, Wu A, Yan H, *et al.* Trapping $[PMo_{12}O_{40}]^{3-}$ clusters into pre-synthesized ZIF-67 toward Mo_xCo_xC particles confined in uniform carbon polyhedrons for efficient overall water splitting. Chem Sci, 2018, 9: 4746–4755
16 Deng S, Yang F, Zhang Q, *et al.* Phase modulation of (1T-2H)-$MoSe_2$ /TiC-C shell/core arrays via nitrogen doping for highly efficient hydrogen evolution reaction. Adv Mater, 2018, 30: 1802223
17 Deng S, Zhong Y, Zeng Y, *et al.* Directional construction of vertical nitrogen-doped 1T-2H $MoSe_2$/graphene shell/core nanoflake arrays for efficient hydrogen evolution reaction. Adv Mater, 2017, 29: 1700748
18 Yin Y, Zhang Y, Gao T, *et al.* Synergistic phase and disorder engineering in 1T-$MoSe_2$ nanosheets for enhanced hydrogen-evolution reaction. Adv Mater, 2017, 29: 1700311
19 Zheng X, Han X, Cao Y, *et al.* Identifying dense $NiSe_2$/$CoSe_2$ heterointerfaces coupled with surface high-valence bimetallic sites for synergistically enhanced oxygen electrocatalysis. Adv Mater, 2020, 32: 2000607
20 Gu B, Dutta S, Hong Y, *et al.* Harmonious heterointerfaces formed on 2D-Pt nanodendrites by facet-respective stepwise metal deposition for enhanced hydrogen evolution reaction. Angew Chem Int Ed, 2023, 62: e202307816
21 Patel A, Vaghasiya J, Chauhan P, *et al.* Synergistic 2D $MoSe_2$@WSe_2 nanohybrid heterostructure toward superior hydrogen evolution and flexible supercapacitor. Nanoscale, 2022, 14: 6636–6647
22 Zong H, Yu K, Zhu Z. Heterostructure nanohybrids of Ni-doped $MoSe_2$ coupled with Ti_2NT_x toward efficient overall water splitting. Electrochim Acta, 2020, 353: 136598
23 Nørskov J, Bligaard T, Logadottir A, *et al.* Trends in the exchange current for hydrogen evolution. J Electrochem Soc, 2005, 152: J23
24 Hinnemann B, Moses P, Bonde J, *et al.* Biomimetic hydrogen evolution: MoS_2 nanoparticles as catalyst for hydrogen evolution. J Am Chem Soc, 2005, 127: 5308–5309
25 Pan H. Tension-enhanced hydrogen evolution reaction on vanadium disulfide monolayer. Nanoscale Res Lett, 2016, 11: 113
26 Xia W, Chen Y, Han M, *et al.* MoC-$MoSe_2$ heterostructures as multifunctional catalyst toward promoting the stepwise polysulfide conversion for lithium-sulfur batteries. Adv Funct Mater, 2024, 34: 2400262
27 Feng S, Li D, Dong H, *et al.* Tailoring the Mo–N/Mo–O configuration in MoO_2/Mo_2N heterostructure for ampere-level current density hydrogen production. Appl Catal B-Environ, 2024, 342: 123451
28 Yang F, Qiao W, Yu L, *et al.* Support engineering modulated Pt/hierarchical $MoSe_2$@mesoporous hollow carbon spheres for efficient methanol-assisted water splitting. Chem Eng J, 2024, 483: 149055
29 Li T, Li J, Zhang L, *et al.* Work-function-induced interfacial electron redistribution of MoO_2/WO_2 heterostructures for high-efficiency electrocatalytic hydrogen evolution reaction. Rare Met, 2024, 43: 489–499

30 Chen H, Yang L, Wang R, *et al.* Constructing CoO/Mo_2C heterostructures with interfacial electron redistribution induced by work functions for boosting overall water splitting. Small, 2023, 19: 2304086
31 Ma X, Yang J, Xu X, *et al.* NiSe/Ni_3Se_2 on nickel foam as an ultra-high-rate HER electrocatalyst: common anion heterostructure with built-in electric field and efficient interfacial charge transfer. RSC Adv, 2021, 11: 34432–34439
32 Chen D, Lu R, Yu R, *et al.* Work-function-induced interfacial built-in electric fields in Os-$OsSe_2$ heterostructures for active acidic and alkaline hydrogen evolution. Angew Chem Int Ed, 2022, 61: e202208642
33 Lv X, Liu X, Suo Y, *et al.* Identifying the dominant role of pyridinic–N–Mo bonding in synergistic electrocatalysis for ambient nitrogen reduction. ACS Nano, 2021, 15: 12109–12118
34 Liu Y, Feng Q, Liu W, *et al.* Boosting interfacial charge transfer for alkaline hydrogen evolution via rational interior Se modification. Nano Energy, 2021, 81: 105641
35 Van der Heijden O, Park S, Eggebeen J, *et al.* Non-kinetic effects convolute activity and tafel analysis for the alkaline oxygen evolution reaction on NiFeOOH electrocatalysts. Angew Chem Int Ed, 2023, 62: e202216477
36 Wang K, Cao J, Yang X, *et al.* Kinetically accelerating elementary steps via bridged Ru-H state for the hydrogen-evolution in anion-exchange membrane electrolyzer. Adv Funct Mater, 2023, 33: 2212321
37 Zhang X, Zhang D, Chen X, *et al.* Te-doped-WSe_2/W as a stable monolith catalyst for ampere-level current density hydrogen evolution reaction. Phys Chem Chem Phys, 2024, 26: 3880–3889
38 Luo Y, Tang L, Khan U, *et al.* Morphology and surface chemistry engineering toward pH-universal catalysts for hydrogen evolution at high current density. Nat Commun, 2019, 10: 269
39 Das M, Jena N, Purkait T, *et al.* Single-phase Ni_5P_4–copper foam superhydrophilic and aerophobic core–shell nanostructures for efficient hydrogen evolution reaction. J Mater Chem A, 2019, 7: 23989–23999
40 Parvin S, Kumar A, Ghosh A, *et al.* An earth-abundant bimetallic catalyst coated metallic nanowire grown electrode with platinum-like pH-universal hydrogen evolution activity at high current density. Chem Sci, 2020, 11: 3893–3902
41 Yang J, Mohmad A, Wang Y, *et al.* Ultrahigh-current-density niobium disulfide catalysts for hydrogen evolution. Nat Mater, 2019, 18: 1309–1314
42 Zheng Z, Yu L, Gao M, *et al.* Boosting hydrogen evolution on MoS_2 via co-confining selenium in surface and cobalt in inner layer. Nat Commun, 2020, 11: 3315
43 Sarwar S, Nautiyal A, Cook J, *et al.* Facile microwave approach towards high performance MoS_2/graphene nanocomposite for hydrogen evolution reaction. Sci China Mater, 2019, 63: 62–74
44 Wang C, Li P, Zong L, *et al.* High-temperature shock enabled synthesis of ultrafine Ru nanoparticles anchoring onto tungsten carbide with strong metal-support interaction for ampere-level current density hydrogen evolution. J Alloys Compd, 2023, 967: 171667
45 Zulqarnain M, Shah A, Khan M, *et al.* $FeCoSe_2$ nanoparticles embedded in g-C_3N_4: a highly active and stable bifunctional electrocatalyst for overall water splitting. Sci Rep, 2020, 10: 6328
46 Chen Y, Yu G, Chen W, *et al.* Highly active, nonprecious electrocatalyst comprising borophene subunits for the hydrogen evolution reaction. J Am Chem Soc, 2017, 139: 12370–12373
47 Wang F, Wu Y, Dong B, *et al.* Robust porous WC-based self-supported ceramic electrodes for high current density hydrogen evolution reaction. Adv Sci, 2022, 9: 2106029
48 Liu H, Yu J, Lin J, *et al.* CeO_2 supported high-valence Fe oxide for highly active and stable water oxidation. EES Catal, 2023, 1: 720–729
49 Zhang C, Luo Y, Tan J, *et al.* High-throughput production of cheap mineral-based two-dimensional electrocatalysts for high-current-density hydrogen evolution. Nat Commun, 2020, 11: 3724
50 Liu R, Gong Z, Liu J, *et al.* Design of aligned porous carbon films with single-atom Co–N–C sites for high-current-density hydrogen generation. Adv Mater, 2021, 33: 2103533
51 Zhang Z, Wang Y, Leng X, *et al.* Controllable edge exposure of MoS_2 for efficient hydrogen evolution with high current density. ACS Appl Energy Mater, 2018, 1: 1268–1275
52 Riyajuddin S, Azmi K, Pahuja M, *et al.* Super-hydrophilic hierarchical Ni-foam-graphene-carbon nanotubes-Ni_2P–CuP_2 nano-architecture as efficient electrocatalyst for overall water splitting. ACS Nano, 2021, 15: 5586–5599
53 Zhang J, Li Y, Xu C, *et al.* 2D/2D/1D structure of a self-supporting electrocatalyst for efficient hydrogen evolution. ACS Appl Energy Mater, 2022, 5: 1710–1719
54 Yang T, Chen Z, Wang Y, *et al. In situ* insertion of silicon nanowires into hollow porous Co/NC polyhedra enabling large-current-density hydrogen evolution electrocatalysis. Small, 2024, 20: e2305873
55 Li G, Yu J, Jia J, *et al.* Cobalt-cobalt phosphide nanoparticles@nitrogen-phosphorus doped carbon/graphene derived from cobalt ions adsorbed saccharomycete yeasts as an efficient, stable, and large-current-density electrode for hydrogen evolution reactions. Adv Funct Mater, 2018, 28: 1801332
56 Zhu L, Lin H, Li Y, *et al.* A rhodium/silicon co-electrocatalyst design concept to surpass platinum hydrogen evolution activity at high overpotentials. Nat Commun, 2016, 7: 12272
57 Wu Y, Su L, Wang Q, *et al. In situ* preparation of $Ni(OH)_2$/$CoNi_2S_4$/NF composite as efficient electrocatalyst for hydrogen evolution reaction. Ionics, 2023, 29: 675–683
58 Nguyen C, Tran T, Truong T, *et al.* MOF-templated synthesis of three-dimensional B-doped NiCoP hollow nanorod arrays for highly efficient and stable natural seawater splitting. ACS Appl Energy Mater, 2023, 6: 10713–10722

Acknowledgement This work was financially supported by the National Natural Science Foundation of China (52002294 and 22379116), Key Scientific Research Program of Department of Education of Hubei Province (D20231501), Graduate Innovative Fund of Wuhan Institute of Technology (CX2023082), City University of Hong Kong Donation Research Grants (DON-RMG 9229021 and 9220061), and City University of Hong Kong Strategic Research Grant (SRG) (7005505).

Author contributions Chen X, Feng S, and Xie S conducted the experiments and analyzed the data; Chen X, Feng S, and Miao Y finished the theoretical calculations; Gao B, Zhang X, Huang L, and Li Y participated in experiments and data analysis; Chen X wrote the paper with support from Feng S; Peng X managed the project; Peng X and Chu P K acquired funding and contributed to the revision of the paper. All authors contributed to the general discussion.

Conflict of interest The authors declare that they have no conflict of interest.

Supplementary information Supplementary materials are available in the online version of the paper.

Xiang Chen received his BS in composite materials and engineering from Hunan Institute of Technology in 2022. He is studying for his master's degree at Wuhan Institute of Technology under the supervision of Prof. Xiang Peng. His research interest is nanostructured transition metal compounds for energy-efficient hydrogen production.

Xiang Peng received his PhD in physics and materials science from City University of Hong Kong in 2017. He was a postdoctoral fellow at City University of Hong Kong from 2017 to 2018. He is currently a professor of materials science and engineering at Wuhan Institute of Technology. His research focuses on the design of functional nanomaterials and their applications in energy storage and conversion.

功函促进钼基异质结电催化剂的电子结构重整提升其析氢反应活性

陈想[1], 冯帅[1], 谢松[1], 苗亚萍[3], 高标[4], 张旭明[4], 黄莉[5], 李筠[5], Paul K. Chu[2], 彭祥[1*]

摘要 Mo基催化剂在电催化析氢反应(HER)中具有巨大应用潜力. 然而, 其活性位点的暴露不足、极强的氢吸附能力导致其催化性能未能充分体现. 本文在碳布上构筑了Mo_2N–$MoSe_2$异质结(MNS), 以增强Mo基催化剂的HER活性. 由于MNS中的Mo_2N具有较低的功函数, 能够在异质界面产生内建电场, 显著提高了其在HER中电荷转移效率. 此外, MNS中原子之间的强电子相互作用优化了Mo位点的电子结构, 降低了氢吸附能力, 进一步增强了其本征催化活性. 因此, MNS催化剂产生20 mA cm^{-2}和1 A cm^{-2}的析氢电流密度所需的过电位仅为65和210 mV, Tafel斜率仅为96 mV dec^{-1}. 此外, MNS在1 A cm^{-2}电流密度下稳定运行240小时后, 形貌、结构和性能均无明显变化. 以上研究结果为工业大电流制氢所需的非贵金属基电催化剂的设计和合成提供了新思路.

Supporting Information

Boosting Hydrogen Evolution via Work-Function-Accelerated Electronic Reconfiguration of Mo-based Heterojunction

Xiang Chen[1], Shuai Feng[1], Song Xie[1], Yaping Miao[3], Biao Gao[4], Xuming Zhang[4], Li Huang[5], Yun Li[5], Paul K. Chu[2] and Xiang Peng[1*]

[1] Hubei Key Laboratory of Plasma Chemistry and Advanced Materials, Engineering Research Center of Phosphorus Resources Development and Utilization of Ministry of Education, School of Materials Science and Engineering, Wuhan Institute of Technology, Wuhan 430205, China

[2] Department of Physics, Department of Materials Science and Engineering, and Department of Biomedical Engineering, City University of Hong Kong, Tat Chee Avenue, Kowloon, Hong Kong, China

[3] School of Textile Science and Engineering, Xi'an Polytechnic University, Xi'an 710048, China

[4] The State Key Laboratory of Refractories and Metallurgy, Institute of Advanced Materials and Nanotechnology, Wuhan University of Science and Technology, Wuhan 430081, China

[5] Guizhou Wujiang Hydropower Development Co, LTD, Guizhou 550002, China

* Correspondence: xpeng@wit.edu.cn (X. Peng)

Supplementary note: TOF calculation

The TOF values are calculated according to the method reported by Jaramillo's group. The per-site TOF is calculated by the following equation:

$$\mathrm{TOF} = \frac{\text{No. of total hydrogen turnovers/cm}^2}{\text{No. of active of sites/cm}^2}.$$

The total number of hydrogen turnovers is calculated from the current density as shown in the following:

$$\text{Number of } \mathrm{H_2} = \left(\text{per}\frac{\mathrm{mA}}{\mathrm{cm^2}}\right)\left(\frac{1\ \mathrm{C\ s^{-1}}}{1000\ \mathrm{mA}}\right)\left(\frac{1\ \mathrm{mol\ e^{-1}}}{96485.3\ \mathrm{C}}\right)\left(\frac{1\ \mathrm{mol\ H_2}}{2\ \mathrm{mol\ e^{-1}}}\right)\left(\frac{6.022\times10^{23}\mathrm{H_2\ mulecules}}{1\ \mathrm{mol\ H_2}}\right) = 3.12 \times 10^{15}\ \frac{\mathrm{H_2\ s^{-1}}}{\mathrm{cm^2}}.$$

The active sites per real surface area are calculated by the following formula:

$$\text{Number of active sites} = \left(\frac{\text{No.of atoms/unit cell}}{\text{Volunme/unit cell}}\right)^{\frac{2}{3}}.$$

The number of active sites of $MoSe_2$-Mo_2N/CC is derived as follows:

$$\text{Number of active sites} \times \mathrm{ECSA} = \left(\frac{\text{No.of atoms/unit cell}}{\text{Volume/unit cell}}\right)^{\frac{2}{3}} \times \mathrm{x} \times \mathrm{ECSA} + \left(\frac{\text{No.of atoms/unit cell}}{\text{Volume/unit cell}}\right)^{\frac{2}{3}} \times \mathrm{y} \times \mathrm{ECSA}$$

where x and y are the molar ratios of $MoSe_2$ and Mo_2N on the surface of the $MoSe_2$-Mo_2N/CC electrodes, respectively.

The unit cell of Mo contains two atoms with a volume of 31.1 $Å^3$, while $MoSe_2$ contains one Mo atom and two Se atom with a volume of 121.1$Å^3$ and Mo_2N contains two Mo atoms and one N atom with a volume of 72.2 $Å^3$. The phase ratio of $MoSe_2$ to Mo_2N is determined by the XPS quantitative analysis using XPSPEAK. MCN contains 86.2% MoC and 13.8% Mo_2N.

(1) $MoSe_2$

$$\text{No. of active sites} = \left(\frac{\text{No. of atoms/unit cell}}{\text{Volunme/unit cell}}\right)^{\frac{2}{3}}$$

$$\text{No. of active sites} = \left(\frac{3\ \text{atoms/unit cell}}{121.1\ \text{Å}^3/\text{unit cell}}\right)^{\frac{2}{3}}$$

No. of active sites = 8.5×10^{14} atoms cm^{-2}.

$$\text{ECSA} = \frac{\text{Specific capacitance } (\mu\text{F cm}^{-2})}{40\ \mu\text{F cm}^{-2}\ \text{per cm}^2_{\text{ECSA}}} = \text{A}_{\text{geo}} \times \frac{22000\ (\mu\text{F cm}^{-2})}{40\ \mu\text{F cm}^{-2}\ \text{per cm}^2_{\text{ECSA}}}$$

$$\text{TOF} = \frac{(3.12 \times 10^{15}\ \frac{\text{H}_2\ \text{s}^{-1}}{\text{cm}^2}) \times |j|}{\text{No. of active sites } \times \text{ECSA}}$$

(2) Mo_2N

$$\text{No. of active sites} = \left(\frac{\text{No. of atoms/unit cell}}{\text{Volunme/unit cell}}\right)^{\frac{2}{3}}$$

$$\text{No. of active sites } (\text{Mo}_2\text{N}) = \left(\frac{3\ \text{atoms/unit cell}}{72.2\ \text{Å}^3/\text{unit cell}}\right)^{\frac{2}{3}}$$

No. of active sites (Mo_2N) = 1.2×10^{15} atoms cm^{-2}

$$\text{ECSA} = \frac{\text{Specific capacitance } (\mu\text{F cm}^{-2})}{40\ \mu\text{F cm}^{-2}\ \text{per cm}^2_{\text{ECSA}}} = \text{A}_{\text{geo}} \times \frac{323000\ (\mu\text{F cm}^{-2})}{40\ \mu\text{F cm}^{-2}\ \text{per cm}^2_{\text{ECSA}}}$$

$$\text{TOF} = \frac{(3.12 \times 10^{15}\ \frac{\text{H}_2\ \text{s}^{-1}}{\text{cm}^2}) \times |j|}{\text{No. of active sites } \times \text{ECSA}}$$

(3) Mo_2N-$MoSe_2$ heterointerface

$$\text{No. of active sites} = \left(\frac{\text{No. of atoms/unit cell}}{\text{Volunme/unit cell}}\right)^{\frac{2}{3}}$$

$$\text{No. of active sites}(\text{MoSe}_2) = \left(\frac{3\ \text{atoms/unit cell}}{121.1\ \text{Å}^3/\text{unit cell}}\right)^{\frac{2}{3}}$$

No. of active sites = 8.5×10^{14} atoms cm^{-2}

$$\text{No. of active sites } (\text{Mo}_2\text{N}) = \left(\frac{3\ \text{atoms/unit cell}}{72.2\ \text{Å}^3/\text{unit cell}}\right)^{\frac{2}{3}}$$

No. of active sites (Mo_2N) = 1.2×10^{15} atoms cm^{-2}

$$\mathrm{ECSA} = \frac{\text{Specific capacitance } (\mu\mathrm{F\ cm^{-2}})}{40\ \mu\mathrm{F\ cm^{-2}}\ \text{per}\ \mathrm{cm^2_{ECSA}}} = \mathrm{A_{geo}} \times \frac{336000\ (\mu\mathrm{F\ cm^{-2}})}{40\ \mu\mathrm{F\ cm^{-2}}\ \text{per}\ \mathrm{cm^2_{ECSA}}}$$

TOF

$$= \frac{(3.12 \times 10^{15}\ \frac{\mathrm{H_2\ s^{-1}}}{\mathrm{cm^2}}\ \text{per}\ \frac{\mathrm{mA}}{\mathrm{cm^2}}) \times |j|}{\text{No. of active sites (MoC)} \times \mathrm{x} \times \mathrm{ECSA} + \text{No. of active sites } (\mathrm{Mo_2N}) \times \mathrm{y} \times \mathrm{ECSA}}$$

where x = 86.2% and y = 13.8%.

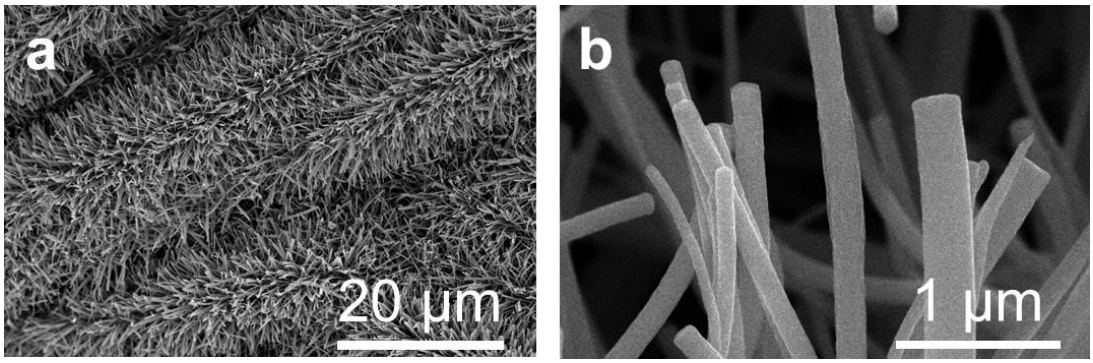

Figure S1. (a-b) SEM images of MN/CC.

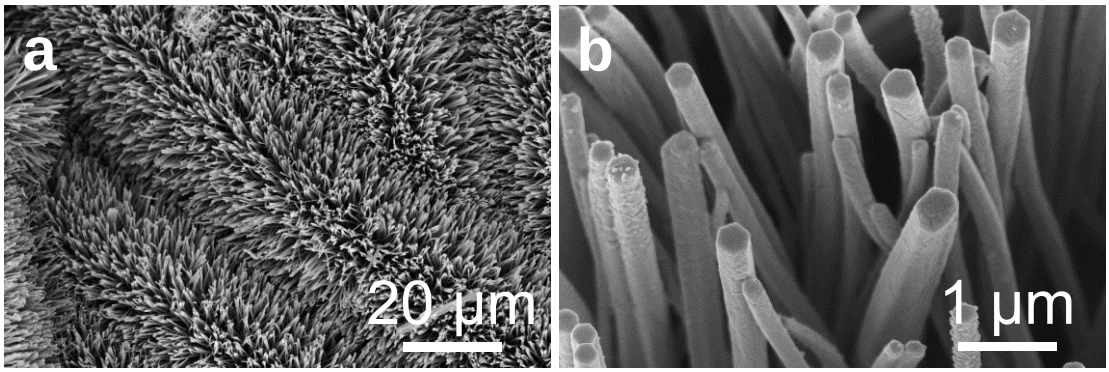

Figure S2. (a-b) SEM images of MS/CC.

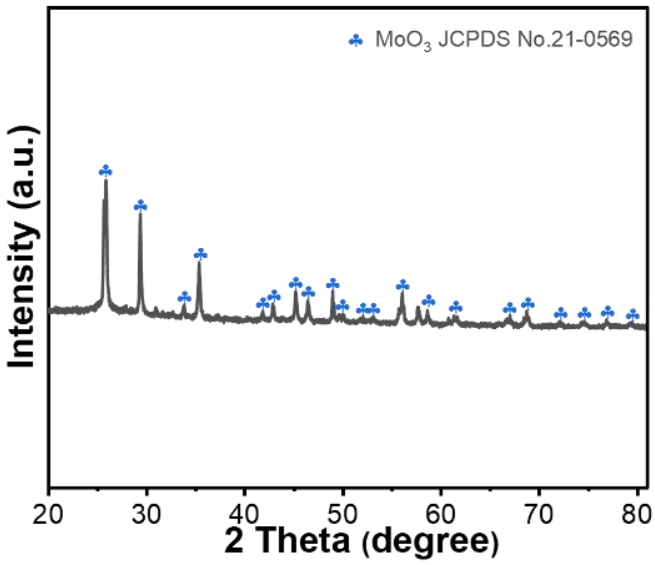

Figure S3. XRD pattern of MoO_3/CC.

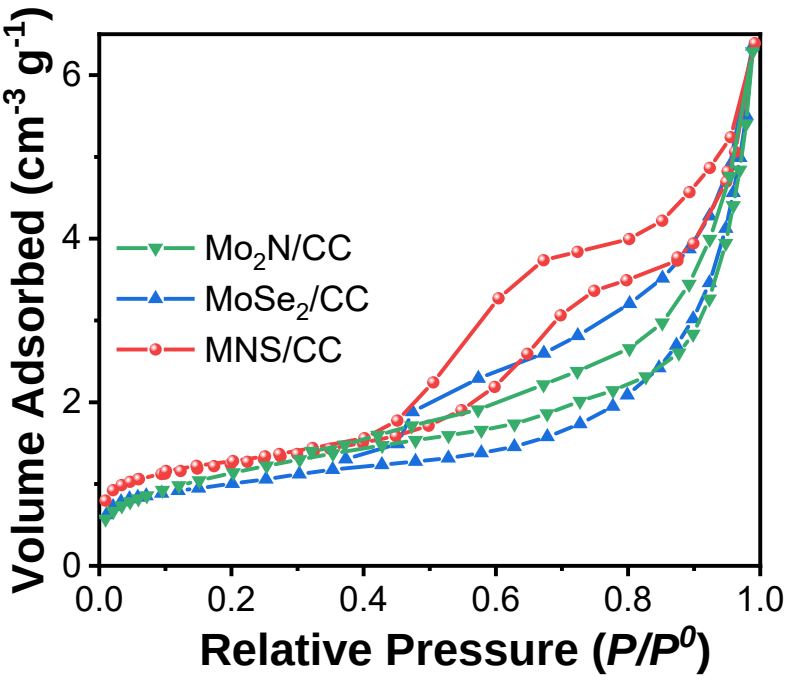

Figure S4. N_2 adsorption-desorption isotherms for Mo_2N/CC, $MoSe_2$/CC, and MNS/CC.

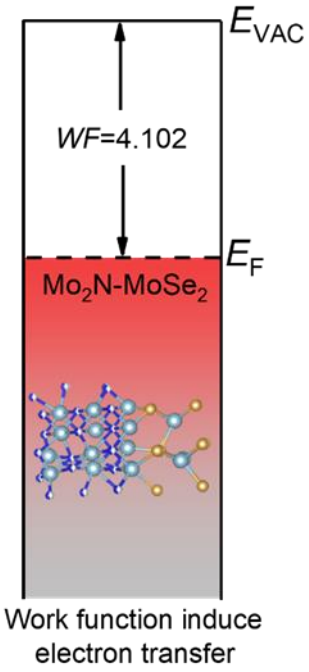

Figure S5. Scheme of the work function for Mo_2N-$MoSe_2$, where E_F and E_{vac} represent the Fermi level and vacuum level, respectively.

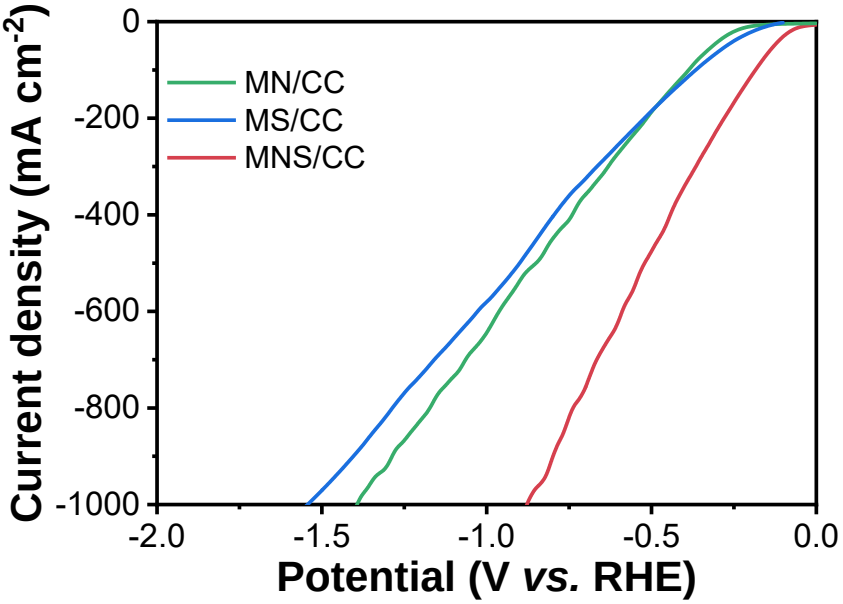

Figure S6. The LSV curves of MN/CC, MS/CC, and MNS/CC without *iR*-correction.

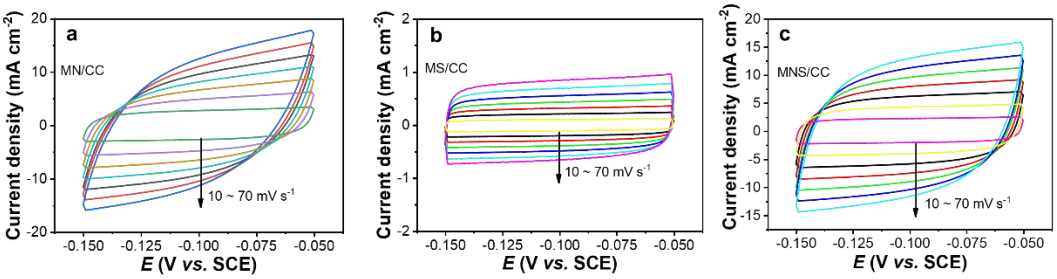

Figure S7. CV curves of (a) MN/CC, (b) MS/CC, and (c) MNS/CC.

Table S1. The concentrations and contents of Mo in Mo_2N/CC, Mo_2N-$MoSe_2$/CC, and $MoSe_2$/CC were quantified through ICP analysis.

	Mo_2N/CC	Mo_2N-Mo_2Se/CC	$MoSe_2$/CC
Mo content (mg g^{-1})	3.50	3.55	3.60
Mo mass loading (mg cm^{-2})	2.800	2.840	2.880

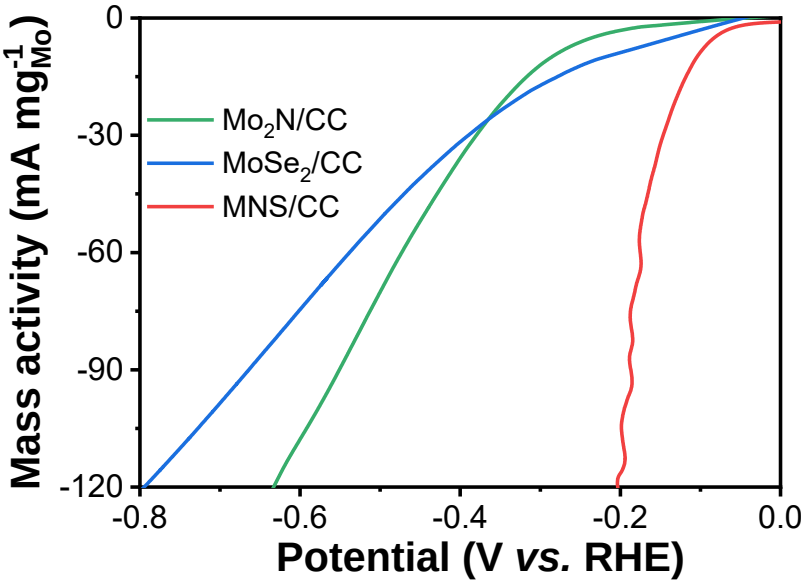

Figure S8. Mass activity of Mo_2N/CC, MNS/CC, and $MoSe_2$/CC based on Mo mass loading.

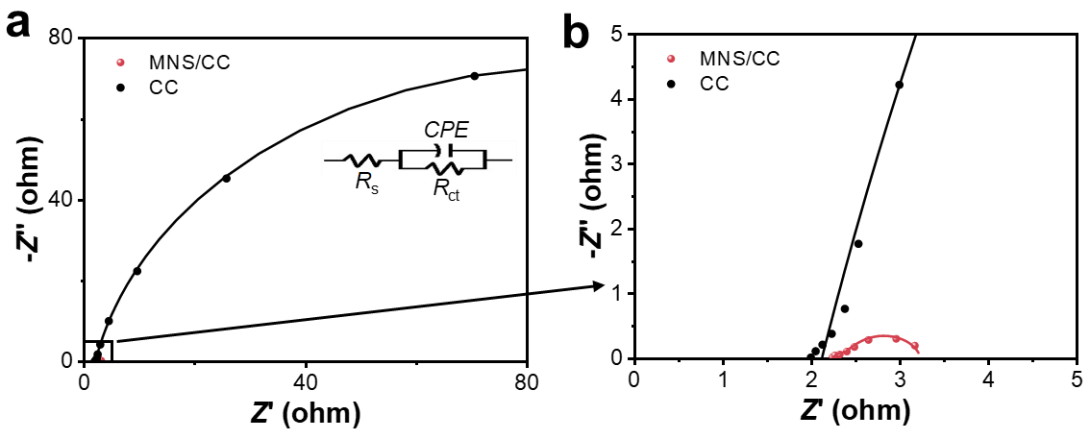

Figure S9. (a) EIS spectra of CC and MNS/CC; (b) An enlarged view of the selected region.

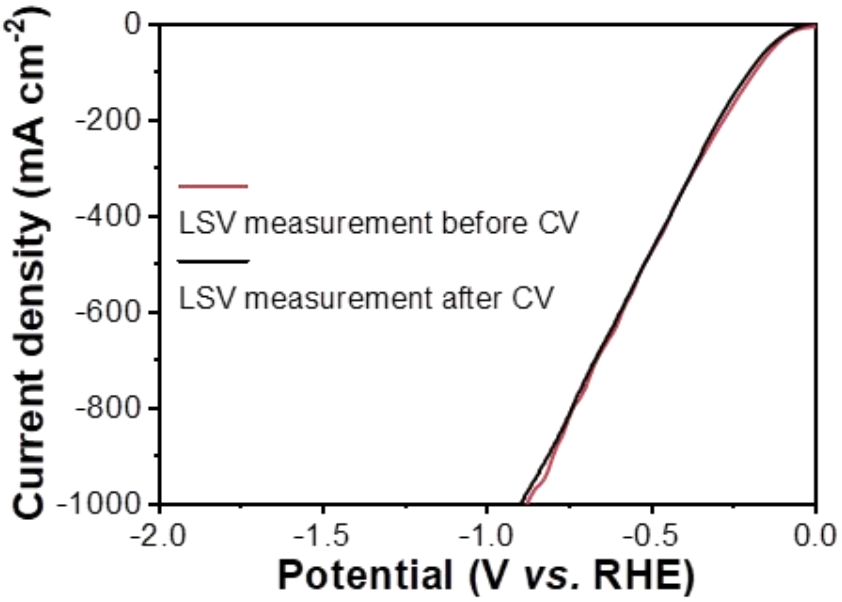

Figure S10. Comparison of LSV curves before and after cyclic voltammetry test.

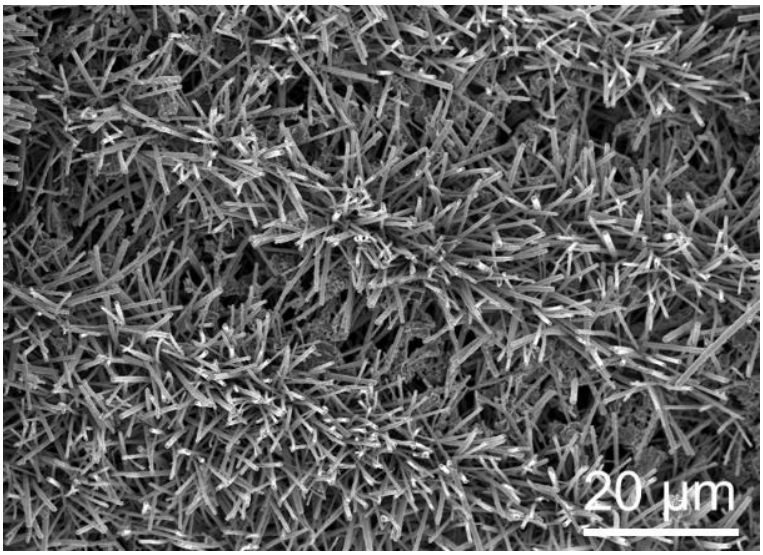

Figure S11. SEM image of MNS/CC after the long-term test.

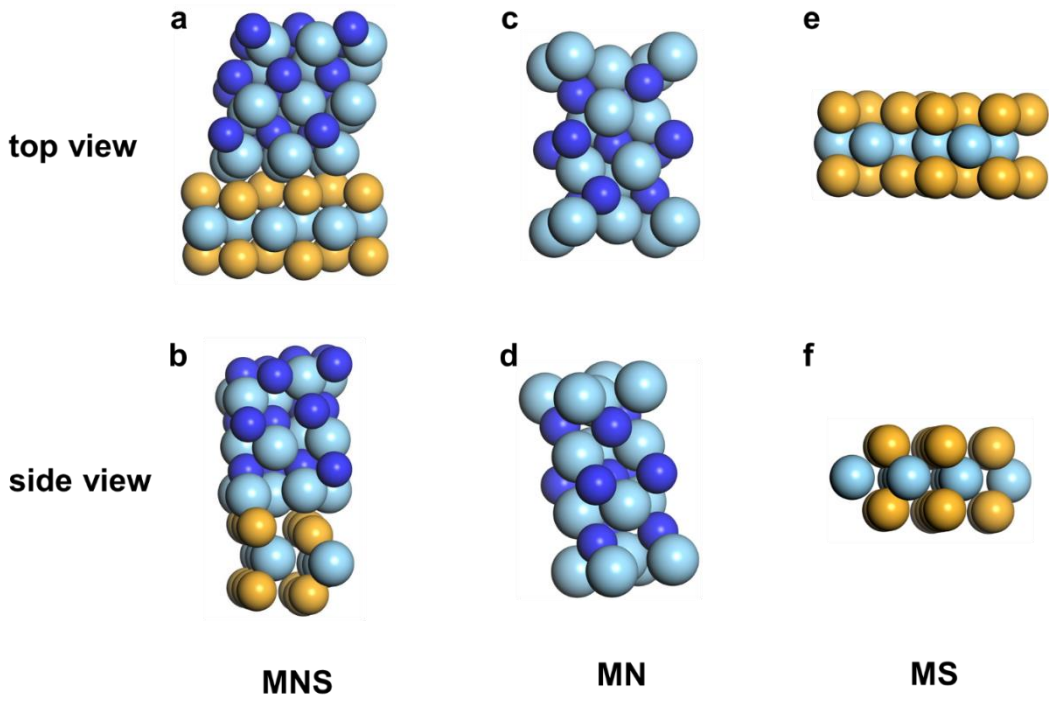

Figure S12. Top and side views of (a-b) MNS, (c-d) Mo_2N, and (e-f) $MoSe_2$ models.

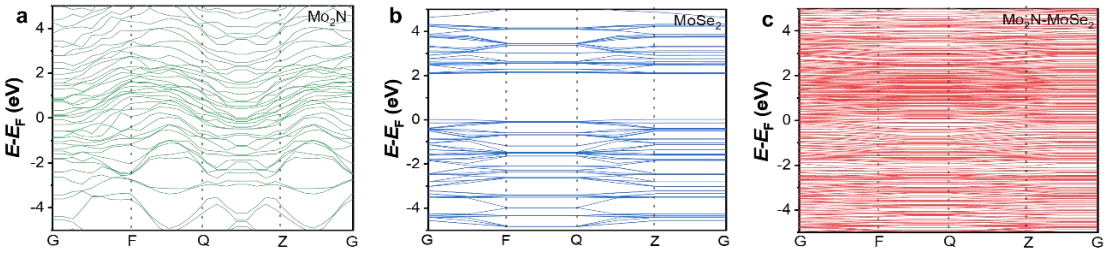

Figure S13. Band structures of (a) Mo_2N, (b) $MoSe_2$, and (c) Mo_2N-$MoSe_2$.

Table S2. HER characteristics of different electrocatalysts in 0.5M H_2SO_4.

Catalysts	η_{1000} [mV]	Refs.
Te-WSe_2	225	[1]
MoS_2/Mo_2C	227	[2]
Ni_5P_4@Cu foam	~230	[3]
Cu-m/Cu-w/NiCo-LDH	246	[4]
MoS_2/graphete	250	[5]
Ru/WC	310	[6]
$Fe_{0.2}Co_{0.8}Se_2$/g-C_3N_4	317	[7]
α-MoB_2	334	[8]
Co-N-C	343	[9]
CoMoP@C	545	[10]
Co/Se-MoS_2-NF	382	[11]
Ni@NCW-2.0	401	[12]
HC-MoS_2/Mo_2C	412	[13]
WC-N/W-1200	420	[14]
MoS_2/CNF	450	[15]
Ni_2P-CuP_2	~500	[16]
Pd_4S/$Pd_3P_{0.95}$	538	[17]
Co/NC-HP@Si-NWs	615	[18]
Co-Co_2P@NPC/rGO	900	[19]
Rh/Si-NWs	950	[20]
40.0 wt% Pt/C	1120	[2]
MNS/CC	226	This work

References

1 Zhang X, Zhang D, Chen X*, et al*. Te-doped-WSe_2/W as a stable monolith catalyst for ampere-level current density hydrogen evolution reaction. Phys Chem Chem Phys, 2024, 26: 3880-3889

2 Luo Y, Tang L, Khan U*, et al*. Morphology and surface chemistry engineering toward pH-universal catalysts for hydrogen evolution at high current density. Nat Commun, 2019, 10: 269

3 Das M, Jena N, Purkait T*, et al*. Single-phase Ni_5P_4-copper foam superhydrophilic and aerophobic core-shell nanostructures for efficient hydrogen evolution reaction. J Mater Chem A, 2019, 7: 23989-23999

4 Parvin S, Kumar A, Ghosh A*, et al*. An earth-abundant bimetallic catalyst coated metallic nanowire grown electrode with platinum-like pH-universal hydrogen evolution activity at high current density. Chem Sci, 2020, 11: 3893-3902

5 Sarwar S, Nautiyal A, Cook J*, et al*. Facile microwave approach towards high performance MoS_2/graphene nanocomposite for hydrogen evolution reaction. Sci China Mater, 2019, 63: 62-74

6 Wang C, Li P, Zong L*, et al*. High-temperature shock enabled synthesis of ultrafine Ru nanoparticles anchoring onto tungsten carbide with strong metal-support interaction for ampere-level current density hydrogen evolution. J Alloys Compd, 2023, 967: 171667

7 Zulqarnain M, Shah A, Khan MA*, et al*. $FeCoSe_2$ Nanoparticles Embedded in

g-C_3N_4: A Highly Active and Stable bifunctional electrocatalyst for overall water splitting. Sci Rep, 2020, 10: 6328

8 Chen Y, Yu G, Chen W, *et al*. Highly Active, Nonprecious Electrocatalyst Comprising Borophene Subunits for the Hydrogen Evolution Reaction. J Am Chem Soc, 2017, 139: 12370-12373

9 Liu R, Gong Z, Liu J, *et al*. Design of Aligned Porous Carbon Films with Single-Atom Co-N-C Sites for High-Current-Density Hydrogen Generation. Adv Mater, 2021, 33: 2103533

10 Yang J, Mohmad AR, Wang Y, *et al*. Ultrahigh-current-density niobium disulfide catalysts for hydrogen evolution. Nat Mater, 2019, 18: 1309-1314

11 Zheng Z, Yu L, Gao M, *et al*. Boosting hydrogen evolution on MoS_2 via co-confining selenium in surface and cobalt in inner layer. Nat Commun, 2020, 11: 3315

12 Liu H, Yu J, Lin J, *et al*. CeO_2 supported high-valence Fe oxide for highly active and stable water oxidation. EES Catal, 2023, 1: 720-729

13 Zhang C, Luo Y, Tan J, *et al*. High-throughput production of cheap mineral-based two-dimensional electrocatalysts for high-current-density hydrogen evolution. Nat Commun, 2020, 11: 3724

14 Wang F, Wu Y, Dong B, *et al*. Robust Porous WC-Based Self-Supported Ceramic Electrodes for High Current Density Hydrogen Evolution Reaction. Adv Sci, 2022, 9: 2106029

15 Zhang Z, Wang Y, Leng X, *et al*. Controllable Edge Exposure of MoS_2 for

Efficient Hydrogen Evolution with High Current Density. ACS Appl Energy Mater, 2018, 1: 1268-1275

16 Riyajuddin S, Azmi K, Pahuja M, *et al*. Super-Hydrophilic Hierarchical Ni-Foam-Graphene-Carbon Nanotubes-Ni_2P-CuP_2 Nano-Architecture as Efficient Electrocatalyst for Overall Water Splitting. ACS Nano, 2021, 15: 5586-5599

17 Zhang J, Li Y, Xu C, *et al*. 2D/2D/1D structure of a self-supporting electrocatalyst for efficient hydrogen evolution. ACS Appl Energy Mater, 2022, 5: 1710-1719

18 Yang L, Yuan X, Liang W, *et al*. One Dimensional MoS_2/MoP Heterostructures for Efficient Electrocatalytic Hydrogen Evolution Reaction. , 2024, 154: 4116-4126

19 Li G, Yu J, Jia J, *et al*. Cobalt-Cobalt Phosphide Nanoparticles@Nitrogen-Phosphorus Doped Carbon/Graphene Derived from Cobalt Ions Adsorbed Saccharomycete Yeasts as an Efficient, Stable, and Large-Current-Density Electrode for Hydrogen Evolution Reactions. Adv Funct Mater, 2018, 28: 1801332

20 Zhu L, Lin H, Li Y, *et al*. A rhodium/silicon co-electrocatalyst design concept to surpass platinum hydrogen evolution activity at high overpotentials. Nat Commun, 2016, 7: 12272